UNITED NATIONS EDUCATIONAL, SCIENTIFIC AND CULTURAL ORGANIZATION
INTERNATIONAL ATOMIC ENERGY AGENCY
INTERNATIONAL CENTRE FOR THEORETICAL PHYSICS
I.C.T.P., P.O. BOX 586, 34100 TRIESTE, ITALY, CABLE: CENTRATOM TRIESTE

H4.SMR/1013-16

SCHOOL ON THE USE OF SYNCHROTRON RADIATION
IN SCIENCE AND TECHNOLOGY:
"John Fuggle Memorial"

3 November - 5 December 1997

Miramare - Trieste, Italy

Atomic Holography with Electrons and X-rays

C. S. Fadley
Lawrence Berkeley Laboratory , California - USA

5

Atomic Holography with Electrons and X-rays

P. M. Len[1], C. S. Fadley[1,2], G. Materlik[3]

[1]*Department of Physics, University of California, Davis, CA 95616 USA*

[2]*Materials Sciences Division, Lawrence Berkeley National Laboratory, Berkeley, CA 94720 USA*

[3]*Hamburger Synchrotronstrahlungslabor (HASYLAB) am Deutsches Elektronen-Synchrotron (DESY), 22603 Hamburg, Germany*

Gabor first proposed holography in 1948 as a means to experimentally record the amplitude and phase of scattered wavefronts, relative to a direct unscattered wave, and to use such a "hologram" to directly image atomic structure. But imaging at atomic resolution has not yet been possible in the way he proposed. Much more recently, Szöke in 1986 noted that photoexcited atoms can emit photoelectron or fluorescent x-ray wavefronts that are scattered by neighboring atoms, thus yielding the direct and scattered wavefronts as detected in the far field that can then be interpreted as holographic in nature. By now, several algorithms for directly reconstructing three-dimensional atomic images from electron holograms have been proposed (*e.g.* by Barton) and successfully tested against experiment and theory. Very recently, Tegze and Faigel, and Gog *et al.* have recorded experimental x-ray fluorescence holograms, and these are found to yield atomic images that are more free of the kinds of aberrations caused by the non-ideal emission or scattering of electrons. The basic principles of these holographic atomic imaging methods are reviewed, including illustrative applications of the reconstruction algorithms to both theoretical and experimental electron and x-ray holograms. We also discuss the prospects and limitations of these newly emerging atomic structural probes.

INTRODUCTION

Historical Origin of Atomic Holography

Dennis Gabor first outlined in 1948 a direct experimental method of recording diffraction phases as well as intensities in an effort to surpass the then current resolution and lens aberration limits of electron microscopy and thus achieve atomic-scale image resolution (1). In Gabor's original scheme, an electron

wavefront (of wavenumber k_0 and wavelength λ_0) diverging from a point focus illuminates an object as well as a detector (or image plate) directly. The interference pattern at this detector involves the wavefronts scattered by the object, and explicitly records the phases of these wavefronts relative to the direct or reference wavefront (Fig. 1(a)). This interference "hologram" thus contains spatial information about the scattering object, which can be retrieved as an image in several ways. Gabor suggested that the developed image plate could simply be re-illuminated by a visible light reference wavefront (of wavenumber k *and wavelength* λ), as shown in Fig. 1(b). The wavefronts thus diffracted by the image plate would create a virtual image of the original object visible to the naked eye, and magnified by a factor of k_0/k. But the image reconstruction can also be performed numerically using a Fourier-transform-like integral, as first pointed out by Wolf (2). Holography is now of course widespread in science and technology, with lasers at usually optical wavelengths providing the reference waves. Note that, since the three-dimensional information of the r-space object field $u(\mathbf{r})$ (shown in Fig. 1 as an optical mask of the letter "F") is "encoded" holographically into a single-wavenumber two-dimensional k-space diffraction pattern $\chi(\hat{\mathbf{k}})$, both a real and twin image of the optical mask are retrieved. This is due to the loss of spatial information perpendicular to the plane of the image plate recording the diffraction pattern, and is by now overcome in optical holography by recording a volume of holographic intensities by means of a thick recording medium (3).

Until recently, Gabor's goal of imaging at atomic resolution had not been attained, due to the lack of a source of sufficiently coherent radiation at such short wavelengths. However, in 1986, Szöke observed that there is an atomic-scale analog of Gabor's holographic scheme: photoexcited atoms produce outgoing photoelectron or fluorescent-x-ray wavefronts, which then reach a far field detector either directly, or after scattering by neighboring atoms surrounding the emitter (5). With a sub-Ångström source size and wavelength, scattered wavefront amplitudes and phases from atoms surrounding the emitter can thus be referenced to the directly emitted wavefront, as shown for the case of fluorescence in Fig. 2(a). It was also pointed out a little later by Barton (4a,4b) and subsequently by Tong *et al.* (4c) that, by measuring diffraction patterns at different wavenumbers, three-dimensional spatial information could be completely encoded into a three-dimensional k-space volume of diffraction intensities $\chi(\mathbf{k})$, from which atomic images free of twin-image effects and other aberrations should be directly obtainable.

Two other approaches for obtaining structural information at the atomic scale should also be mentioned, as illustrated in Fig. 3. First, atomic order and electron density maps can be determined by so-called direct methods from the kinematical (single-scattering) diffraction technique, which exploits the translational symmetry (Bragg planes) of a crystal (6) (Fig. 3(a)). The second is the use of multiple, dynamical scattering from single crystals to solve the phase

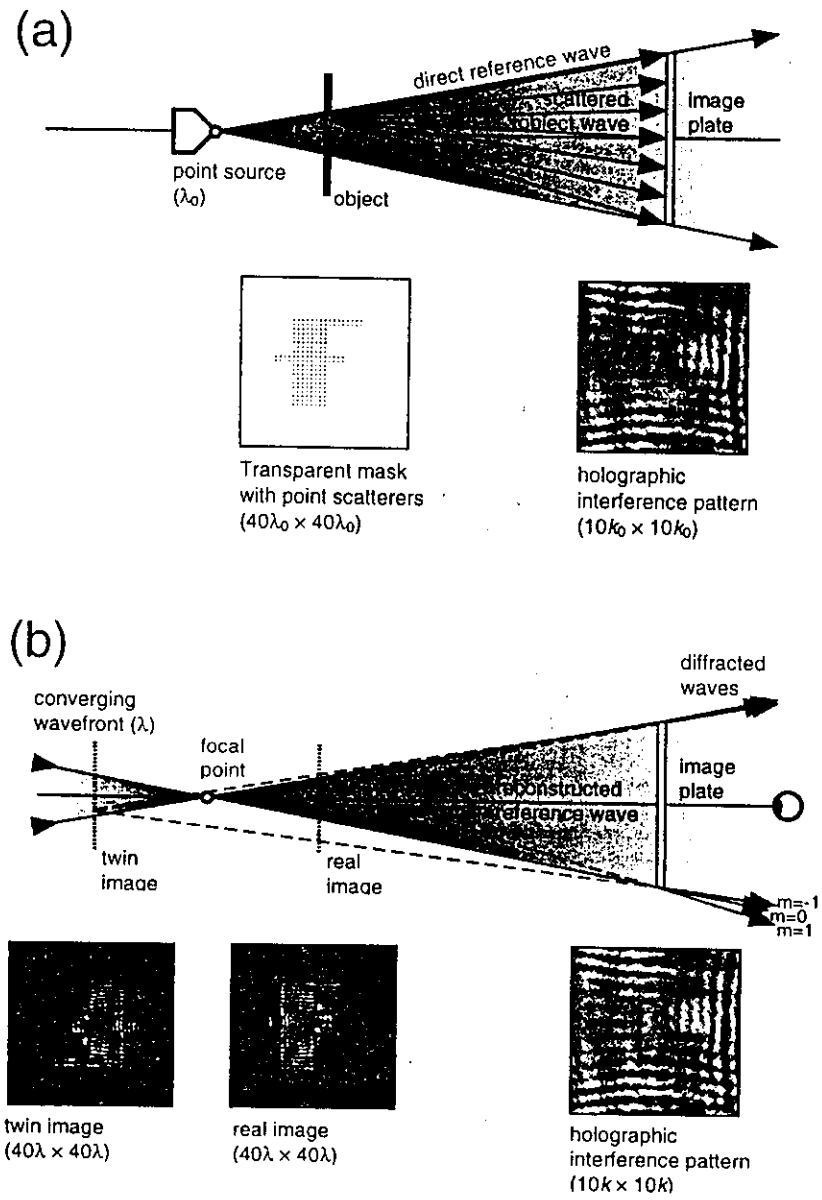

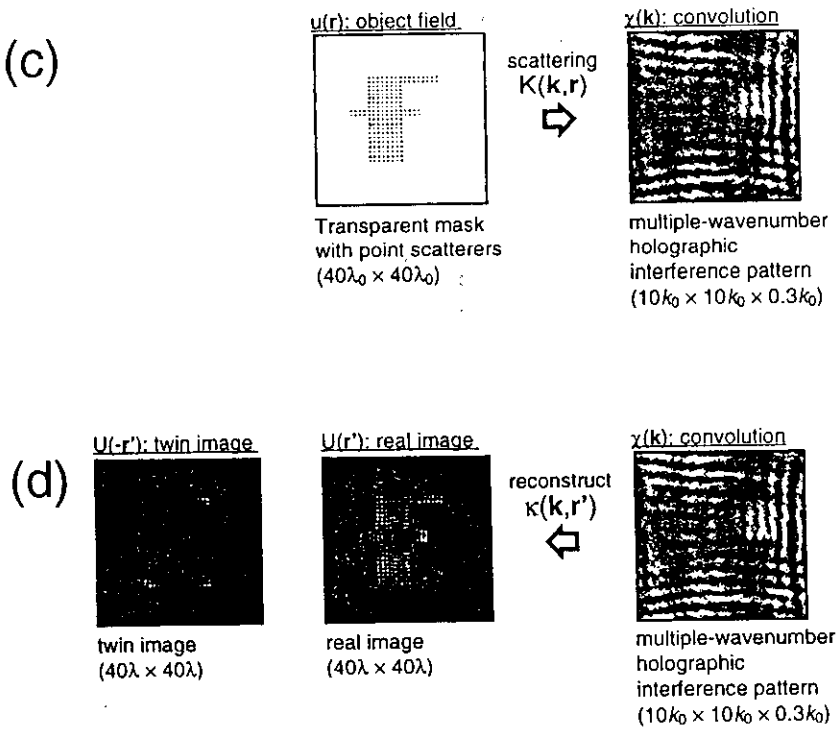

FIGURE 1. (a)-(b) An idealized numerical demonstration of the creation and inversion of single-wavenumber optical Gabor in-line holograms. (a) A point source of coherent radiation at the origin illuminates a transparent mask with point scatterers creating the letter "F" at **r**, as well as an image plate. This image plate is then exposed by a direct wavefront, as well as by the wavefronts scattered by the mask, which produces a holographic interference pattern. (b) The developed image plate is later *re*-illuminated by a reference wavefront. The wavefronts diffracted by the image plate produce a virtual (real) image of the mask at **r**, and a virtual conjugate twin image at the inverse position **-r**. (c)-(d) An analogous demonstration of the creation and inversion of optical multiple-wavenumber holograms. (c) A multiple-wavenumber normalized $\chi(\mathbf{k})$ hologram data set (of which one wavenumber is shown) is calculated from the object field $u(\mathbf{r})$ by means of an **r**-space convolution, using a kernel $K(\mathbf{k},\mathbf{r})$ that describes the emission and scattering physics involved (here, optical scattering in the far field regime). (d) The object field $u(\mathbf{r})$ is recovered as an image intensity $U(\mathbf{r}')$ by a **k**-space deconvolution of $\chi(\mathbf{k})$, using a kernel $\kappa(\mathbf{k},\mathbf{r}')$ that is sufficiently orthogonal to $K(\mathbf{k},\mathbf{r})$. Note that the conjugate twin image $U(\mathbf{r} = -\mathbf{r}')$ has been suppressed, due to the volume of **k**-space enclosed in the multiple-wavenumber $\chi(\mathbf{k})$ considered here.

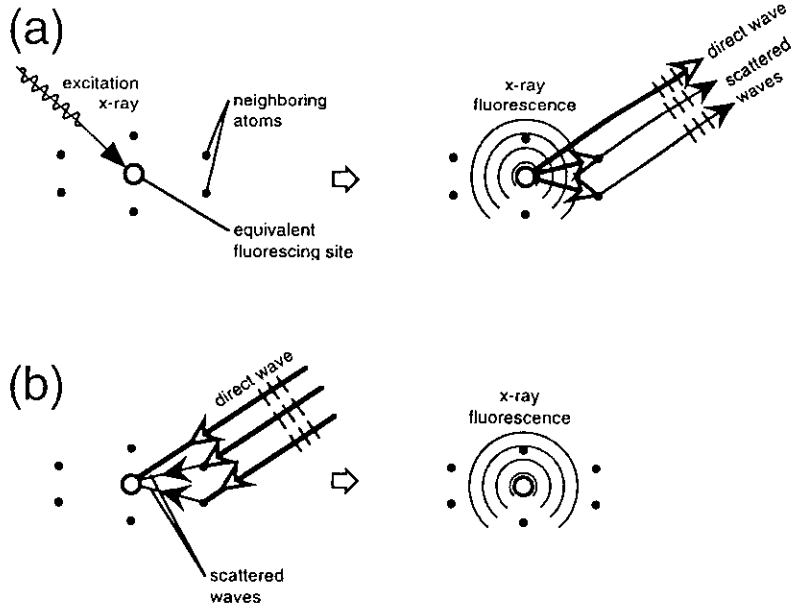

FIGURE 2. Atomic-scale analogs of Gabor holography. (a) The first scheme suggested by Szöke (5), in which an excitation x-ray first creates an inner-shell hole in one of many equivalent fluorescing atoms, and this atom then emits fluorescent x-ray (or electron) wavefronts that illuminate neighboring atoms, as well as a far field detector. This detector senses the interference between the direct wavefront and wavefronts scattered by the neighboring atoms. Moving the detector over a large solid-angle range builds up a holographic interference pattern. (b) The time-reversed case of (a) as suggested by Gog *et al.* (15), where a coherent far field excitation x-ray illuminates and photoexcites an emitter, and also illuminates and is scattered from atoms neighboring the emitter. The emitting atom senses the interference between the direct wavefront and wavefronts elastically scattered by the neighboring atoms. The net photoexcitation is then detected by a stationary, large solid-angle detector. Moving the far field source over a large solid-angle range builds up a holographic interference pattern. In both (a) and (b), atomic images can be reconstructed numerically.

problem of crystallography (7-9), either via Kossel lines (Fig. 3(b)) (10) or standing-wave methods (Fig. 3(c)) (11). The holographic approach is different from these two methods in that it uses the interference pattern which results from the direct unscattered wavefront emitted by a source atom, and the wavefronts which have been singly scattered from neighboring atoms. This does not require translational order (only rotational alignment) between the atomic neighborhoods to be imaged.

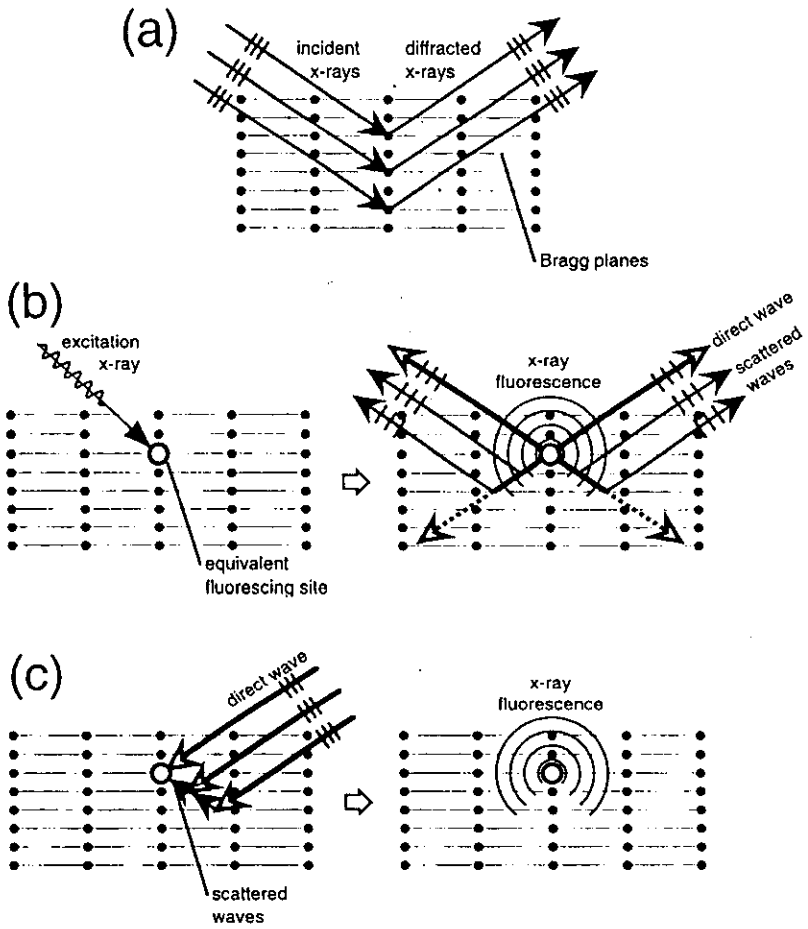

FIGURE 3. Diffraction probes of atomic structure related to atomic holography. (a) Conventional x-ray crystallography, where x-rays are diffracted by Bragg planes of atoms. Diffraction phases are determined by the simultaneous analysis of many Bragg intensities and other methods. (b) Kossel patterns (or Kikuchi bands, for the case of electrons). Fluorescent x-rays (or electrons) from a photoexcited emitter are diffracted by Bragg planes of atoms. Diffraction phases are thus here directly referenced to the unscattered portion of the fluorescence. (c) X-ray standing waves. This is the optical reciprocal of (b), where a coherent plane wave illuminates a fluorescing atom either directly, or after being scattered by Bragg planes of atoms. The interference between these wavefronts determines the amount of fluorescence by the emitter. Note that in all these above cases, the structure to be determined must have long-range atomic order, in contrast to the methods illustrated in Fig. 2.

Basic Principles of Atomic Holography

The process by which three-dimensional atomic image intensities are numerically reconstructed is to first measure the intensity $I(\mathbf{k})$ from a localized source over some range of directions $\hat{\mathbf{k}} = \mathbf{k}/k$ and perhaps also some range of wavenumbers k. Normalized holographic intensities $\chi(\mathbf{k})$ are then derived from either $[I(\mathbf{k})-I_0(\mathbf{k})]/\sqrt{I_0(\mathbf{k})}$ or $[I(\mathbf{k})-I_0(\mathbf{k})]/I_0(\mathbf{k})$, where $I(\mathbf{k})$ is the raw measured intensity, and $I_0(\mathbf{k})$ is the intensity that would be measured in the absence of atomic scattering; that is, $I_0(\mathbf{k})$ is the unperturbed intensity of the reference wave. The overall imaging process can be understood by first considering the hologram to be a convolution of the r-space object field $u(\mathbf{r})$:

$$\chi(\mathbf{k}) = \iiint_R d^3\mathbf{r}\cdot K(\mathbf{k},\mathbf{r})u(\mathbf{r}) + \iiint_R d^3\mathbf{r}\cdot K^*(\mathbf{k},\mathbf{r})u^*(\mathbf{r}), \tag{1}$$

where the convolution kernel $K(\mathbf{k},\mathbf{r})$ somehow describes the physics of the emission and atomic scattering of the photoexcited wavefronts, and R denotes the volume in real space over which the object exists. This produces a three-dimensional $\chi(\mathbf{k})$ volume in k-space, so as to completely encode three-dimensional spatial information of the object field $u(\mathbf{r})$. The reconstruction algorithm is then most simply a k-space deconvolution of $\chi(\mathbf{k})$ to obtain a real-space $U(\mathbf{r}')$ image intensity:

$$U(\mathbf{r}') \equiv \iiint_K d^3\mathbf{k}\cdot\kappa^*(\mathbf{k},\mathbf{r}')\chi(\mathbf{k}), \tag{2}$$

where the reconstruction kernel $\kappa(\mathbf{k},\mathbf{r}')$ has been chosen to be orthogonal to the scattering kernel $K(\mathbf{k},\mathbf{r})$, as integrated over a sufficiently large k-space volume, that is, so that:

$$\begin{aligned} &\iiint_K d^3\mathbf{k}\cdot\kappa^*(\mathbf{k},\mathbf{r}')K(\mathbf{k},\mathbf{r}) \propto \delta(\mathbf{r}-\mathbf{r}'), \\ &\iiint_K d^3\mathbf{k}\cdot\kappa^*(\mathbf{k},\mathbf{r}')K^*(\mathbf{k},\mathbf{r}) \approx 0 \end{aligned} \tag{3}$$

If such a $\kappa(\mathbf{k},\mathbf{r}')$ can be found, then the object field $u(\mathbf{r})$ can thus be recovered as the image intensity $U(\mathbf{r}')$ from Eqs. (1)-(3):

$$\begin{aligned} U(\mathbf{r}') &= \iiint_R d^3\mathbf{r}\cdot\left[u(\mathbf{r})\iiint_K d^3\mathbf{k}\cdot\kappa^*(\mathbf{k},\mathbf{r}')K(\mathbf{k},\mathbf{r}) + u^*(\mathbf{r})\iiint_K d^3\mathbf{k}\cdot\kappa^*(\mathbf{k},\mathbf{r}')K^*(\mathbf{k},\mathbf{r})\right] \\ &= \iiint_R d^3\mathbf{r}'u(\mathbf{r})\delta(\mathbf{r}-\mathbf{r}') \\ &= u(\mathbf{r}'). \end{aligned} \tag{4}$$

So once the emission and scattering process that creates $\chi(\mathbf{k})$ can be sufficiently modeled by a $K(\mathbf{k},\mathbf{r})$ convolution kernel, then a deconvolution kernel $\kappa(\mathbf{k},\mathbf{r}')$ can in principle be formulated so as to directly reconstruct atomic images using Eq. (2).

Atomic Holography Reconstruction

The basic algorithms used in reconstructing atomic holographic images can be understood in the context of a single scattering (or kinematical) model of the scattering process. We consider e^{-ikr}/kr to represent the photoexcited electron or x-ray spherical wavefront that illuminates the (point-like) scattering atoms surrounding the emitter (with the emitted wave assumed to be isotropic for simplicity), $f(\Theta_r^k)$ to be the complex plane-wave atomic scattering factor ($\equiv |f(\Theta_r^k)|\exp[i\psi(\Theta_r^k)]$), where Θ_r^k is the scattering angle, and $\mathbf{k}\cdot\mathbf{r}$ is the phase of the scattered portion of this wavefront as it reaches the far field detector (Fig. 4). Thus the total geometrical path-length phase difference between the reference and scattered wavefronts is $(\mathbf{k}\cdot\mathbf{r} - kr)$. The convolution kernel for this scattering process can then be expressed as:

$$K(\mathbf{k},\mathbf{r}) = \frac{f(\Theta_r^k)}{kr} e^{i(\mathbf{k}\cdot\mathbf{r}-kr)}. \qquad (5)$$

This choice for $K(\mathbf{k},\mathbf{r})$ does not include any allowance for anisotropy in magnitude or phase of the outgoing reference wave, which for the simple example of s-level photoemission, takes the form of an additional factor of $\boldsymbol{\varepsilon}\cdot\mathbf{k}$, where $\boldsymbol{\varepsilon}$ is the polarization vector of the radiation (12). Thus, in photoemission, reference wave anisotropy is almost always present. However, for the case of Kα x-ray fluorescence to be considered below, the outgoing reference wave should be isotropic *and* randomly polarized, and thus be well described by Eq. (5).

Another advantage of x-rays lies in the nature of $f(\Theta_r^k)$. Figure 5 shows the magnitudes and phases of Ni atomic scattering factors for both x-rays and electrons with wavelength $\lambda = 0.79$Å (or wavenumber $k = 8.0$Å^{-1}). Note that the x-ray scattering factors (Fig. 5(a)) are much weaker (by ~1/2000) and more nearly constant in magnitude than those for electrons (Fig. 5(b)), and that the scattering phase shifts for x-rays are also much smaller (by ~1/100) and more nearly constant than those for electrons. Thus, for x-rays $|f(\Theta_r^k)| \approx$ constant $= f_0$, and $\psi(\Theta_r^k) \approx \psi_0 \approx 0$, such that the simplest possible optical scattering kernel results: $K_O(\mathbf{k},\mathbf{r}) \propto e^{i(\mathbf{k}\cdot\mathbf{r}-kr)}$. The reconstruction kernel that is most simply orthogonal to this optical scattering kernel is thus $\kappa_O(\mathbf{k},\mathbf{r}') \equiv e^{i(\mathbf{k}\cdot\mathbf{r}'-kr')}$, as first suggested by Barton and Terminello (4b). Thus for the scattering of fluorescent x-rays, the

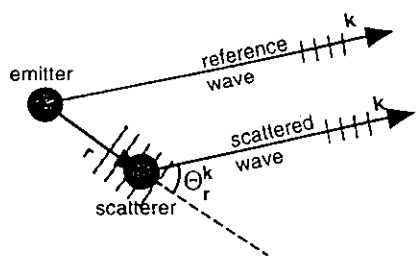

FIGURE 4. Scattering geometry between a photoemitter and a neighboring scattering atom. The photoemitter is placed at the origin, while the scatterer is located at the relative position **r**. The far field detector lies in the direction **k**. The portion of the direct wavefront that is scattered by the neighboring atom into the detector at **r** depends on the scattering angle Θ_r^k between **r** and **k** according to the complex phase factor $f(\Theta_r^k)$.

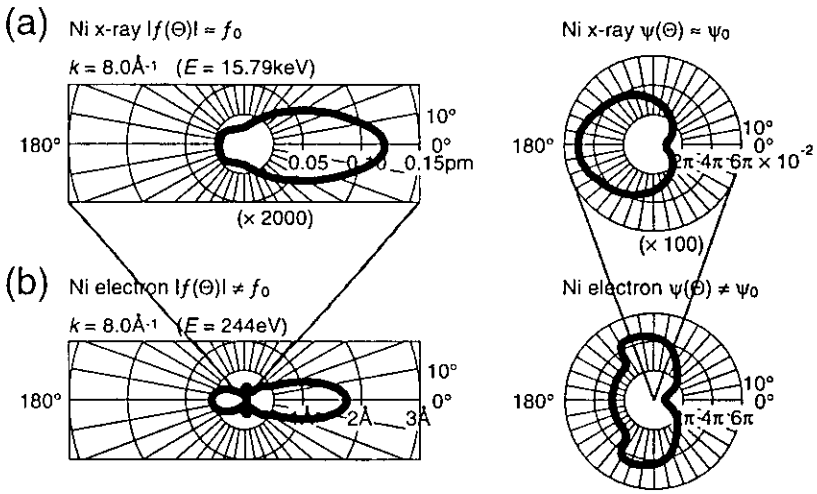

FIGURE 5. Ni scattering factor magnitudes ($|f(\Theta_r^k)|$) and phases ($\psi(\Theta_r^k)$), as a function of scattering angle Θ_r^k for (a) k = 8.0 Å^{-1} (E = 15.79keV) x-rays. (b) k = 8.0 Å^{-1} (E = 244eV) electrons. Θ_r^k = 0° is the forward scattering direction, Θ_r^k = 180° is the backscattering direction.

reconstruction algorithm of Eq. (2) becomes to a good approximation:

$$U(\mathbf{r}') \equiv \iiint_k d^3\mathbf{k}\cdot e^{-i(\mathbf{k}\cdot\mathbf{r}'-kr')}\chi(\mathbf{k}). \qquad (6)$$

This simple optical reconstruction algorithm has been used recently to obtain direct atomic images from experimental single-wavenumber (13,14) and multiple-

wavenumber (15,16) x-ray holographic data sets, as discussed further below.

For example, Fig. 1(c) schematically shows the optical holographic $\chi(\mathbf{k})$ intensities that were numerically calculated from the transparent "F" mask using Eqs. (1) and (5), over a range of different directions ($\hat{\mathbf{k}}$) and wavenumbers (k). Figure 1(d) shows the numerically reconstructed real and twin images obtained from the volume $\chi(\mathbf{k})$ of Fig. 1(c). Due to the three-dimensional spatial information that was encoded in the k-space volume encompassed by $\chi(\mathbf{k})$, the reconstruction algorithm of Eq. (6) suppresses the spurious twin image, while increasing the fidelity of the desired real image (*cf.* Fig. 1(b)).

The optical reconstruction algorithm of Eq. (6) was in fact first used to reconstruct data from electron holographic data sets, *e.g.* from photoelectron diffraction (17-21). However, because of the generally anisotropic nature of the photoemitted source wave, and the strong, non-optical and often multiple nature of electron scattering, the single-scattering optical convolution kernel $K_o(\mathbf{k},\mathbf{r}') \propto e^{i(\mathbf{k}\cdot\mathbf{r}'-kr')}$ does not accurately describe the process by which electron holograms are produced, and consequently the optical reconstruction kernel $\kappa_o(\mathbf{k},\mathbf{r}') = e^{i(\mathbf{k}\cdot\mathbf{r}'-kr')}$ will not in general satisfy the orthogonality condition (Eq. (3)) for electrons. Thus Eq. (6), when applied to electron holograms, often results in images which suffer from aberrations and position shifts (22-24). Nonetheless, useful atomic structure information has been derived from electron holography, with various modifications to the basic optical reconstruction kernel $\kappa_o(\mathbf{k},\mathbf{r}')$, and to the definition of the reconstruction integral (Eq. (2)) itself being proposed (25-29), and comparative reviews of different methods appearing elsewhere (30,31).

In summary, the atomic scattering of x-rays is much more nearly ideal than that of electrons, and this suggests that a simple optical reconstruction kernel as in Eq. (6) can be straightforwardly used to directly obtain atomic images from holographic x-ray intensities. However, more sophisticated reconstruction kernels and deconvolution integrals will probably be necessary to account for the non-ideal nature of the propagation and scattering of electrons, in order to successfully obtain the most accurate atomic images from holographic electron intensities, as discussed elsewhere (25-31).

ATOMIC ELECTRON HOLOGRAPHY

In this section, we discuss the results of applying the imaging algorithm of Eq. (6) to experimental and theoretical photoelectron diffraction results for W 4*f* emission from the surface atoms of clean W(110), with the experimental data being obtained by Denlinger, Rotenberg, and co-workers at Beamline 7.0 of the Advanced Light Source at the Lawrence Berkeley National Laboratory (31). The 4*f* photoelectron peak (which contains *d* and *g* components due to the dipole selection rule) can be resolved into bulk and surface core-level-shifted components, of which atomic images reconstructed from only surface photoemission will be considered here. Photoelectron spectra were measured for kinetic energies of E = 41eV to 197eV (wavenumbers k = 3.3Å^{-1} to 7.2Å^{-1}), and collected over a polar takeoff angle range of $14° \le \theta \le 90°$ ≡ normal emission. These data points were measured at wavenumber intervals corresponding to δk = 0.1Å^{-1}, and angular intervals of $(\delta\theta,\delta\phi) = (3°, 3°\cos\theta)$ corresponding roughly to equal solid angle elements, making a total of 12,280 unique measurements in a symmetry-reduced 1/4th of the total solid-angle above the sample. For each different wavenumber and direction, the W 4*f* peak was resolved into bulk and surface emission components by integrating the areas under the lower and higher flanks of the bulk and surface W 4*f* peaks, respectively, as shown in Fig. 6(a). Figures 6(b)-(c) show the bulk and surface $I(\mathbf{k})$ data sets in k-space, respectively, as viewed down along $[\bar{1}\,\bar{1}\,0]$. Data points in the lower right quadrant have been cut away to reveal the intensities $I(\mathbf{k})$ for the minimum k = 3.3Å^{-1}; the other quadrants show the intensities $I(\mathbf{k})$ for the maximum k = 7.2Å^{-1}. The dark bands at the perimeter indicate the locations in k-space on these iso-wavenumber surfaces where data was not collected. Due to the strong atomic scattering of electrons, the anisotropy of the raw $I(\mathbf{k})$ data, which we measure as $\Delta I / I_0 \equiv (I_{max} - I_{min}) / I_0$, is found to be ≈ 30%, and is easily discernible with this gray scale.

In order to determine the normalized $\chi(\mathbf{k})$ from the raw $I(\mathbf{k})$ intensities of Figs. 6(b)-(c), $I_0(\mathbf{k})$ was determined by fitting a low order polynomial in wavenumber k and polar angle θ to $I(\mathbf{k})$:

$$I_0(\mathbf{k}) = a_{00} + \sum_{m=1}^{3}\sum_{n=1}^{3} a_{mn} k^m \cos\left[(2n-1)\theta\right], \qquad (11)$$

where the coefficients a_{mn} are determined by a least-squares fit to $I(\mathbf{k})$. This is in contrast to previous more approximate methods for determining $I_0(\mathbf{k})$ where simple linear, low-order polynomial, or spline fits were separately made for each set of different wavenumbers along a given direction: $I_{\hat{\mathbf{k}}}(\hat{\mathbf{k}})$, or each set of different directions at a given wavenumber: $I_{\hat{\mathbf{k}}}(k)$. Such separate normalizations within each scanned-wavenumber or scanned-angle set of data points in $I(\mathbf{k})$ arose from the historical development of electron holography, in which data tended to be collected with k-space resolution that was either fine-in-direction/coarse-in-wavenumber or coarse-in-direction/fine-in-wavenumber (30,31). There has in fact been a recent proposal to consider these k-space sampling choices as distinct atomic structure probes (17(e)), but these choices simply represent extremes of a continuous range of k-space sampling, of which the optimal choice has been shown to be in the intermediate range of roughly equally resolved direction and wavenumber data steps (30). Thus, this distinction (17(e)) is artificial, and not

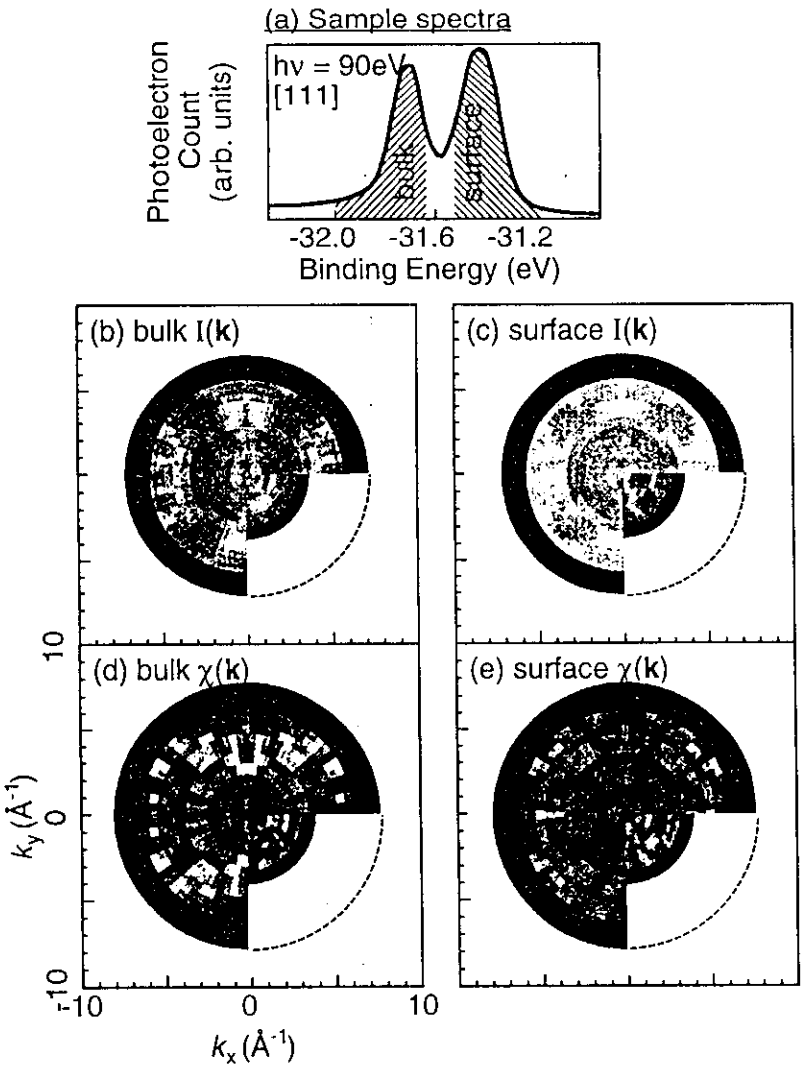

FIGURE 6. (a) Example W $4f_{7/2}$ photoelectron spectrum from clean W(110), with the bulk and surface emitter contributions used to generate the I(k) intensity data points of (b)-(c) shaded in. (b)-(c) Schematic k-space representations of the raw I(k) intensity data sets for bulk and surface W $4f_{7/2}$ emission, respectively. (d)-(e). Normalized bulk and surface emission χ(k) data sets, respectively, corrected for the unscattered intensity I_0 (as derived from Eq. (11)) and an inner potential of V_0 = 14V.

consistent with the optimal use of the holographic methodology. As a consequence, the normalization of $I(\mathbf{k})$ intensities should ideally be made via the determination of a general wavenumber and direction dependent $I_0(\mathbf{k})$ background, as done here, rather than determined separately for each wavenumber or direction in the $I(\mathbf{k})$ data set.

Figures 6(d)-(e) show the normalized bulk and surface $\chi(\mathbf{k})$ functions obtained from the raw $I(\mathbf{k})$ intensities of Figs. 7(b)-(c), using the wavenumber and angle fit $I_0(\mathbf{k})$ of Eq. (11), and after correcting for an inner potential of V_0 = 14V (32) to yield electron wavenumbers and directions beneath the surface of the sample. These data points were then remapped to a δk = 0.1Å^{-1}, and $(\delta\theta,\delta\phi)$ = (5°,5°) grid over the range k = 3.85Å^{-1} to 7.45Å^{-1} (E = 56eV to 211eV), and 40° ≤ θ ≤ 90° range, for a final total of 6,697 unique intensities in the symmetry-reduced 1/4th of the solid angle above the sample.

For comparison, single-scattering and multiple-scattering models were used to calculate the surface emission I(k) from a theoretical W(110) cluster (33). These theoretical photoemission intensities were then also normalized using Eq. (11).

Figure 7 shows the reconstructed images in the vertical $(\bar{1}1\bar{2})$ plane obtained from applying the optical reconstruction kernel of Eq. (6) to: (a) the experimental surface emission $\chi(\mathbf{k})$ of Fig. 6(e); (b) the theoretical single-scattering $\chi(\mathbf{k})$; and (c) the theoretical multiple-scattering $\chi(\mathbf{k})$. The expected atomic image resolution for this wavenumber and angular range of $\chi(\mathbf{k})$ in the horizontal $[\bar{1}11]$ direction is given by $\delta x \approx \pi/\Delta k_x \equiv \pi/(2k_{max}sin(\theta_{max}-\theta_{min})) \approx 0.3$Å, and in the vertical [110] direction is given by $\delta z \approx \pi/\Delta k_z \equiv \pi/(k_{max}-k_{min}\cos(\theta_{max}-\theta_{min})) \approx 0.6$Å (34), and these numbers are comparable to the actual atomic image resolutions in Fig. 7. As noted above, Eq. (6) makes no special effort to suppress aberrations due to the non-optical nature of the electron scattering process. In all of these images, the $\bar{1}\bar{1}0$ backscattering atom and the $\frac{1}{2}\frac{\bar{1}}{2}\frac{\bar{1}}{2}$ and $\frac{\bar{1}}{2}\frac{1}{2}\frac{1}{2}$ side scattering atoms are well-resolved, with experiment and the more accurate multiple-scattering theory showing the sharpest features for the backscattering atoms. In the experimental image of Fig. 7(a), the $\frac{1}{2}\frac{\bar{1}}{2}\frac{\bar{1}}{2}$ and $\frac{\bar{1}}{2}\frac{1}{2}\frac{1}{2}$ atoms are shifted in toward the emitter (by ≈ 0.7Å), and downward from the z = 0Å surface (by ≈ 0.2Å), this is probably primarily due to anisotropies in the photoemitted source wave and the atomic scattering factor for such side-scattering directions. As expected, the backscattering $\bar{1}\bar{1}0$ atom is better resolved due to the more ideal nature of electron backscattering (*cf.* Fig. 5), with no significant position shift. The experimental backscattering image is also less intense (≈50%) than the side scattering atomic images; and image intensities above and below z = -3.5Å have been scaled accordingly. This difference in relative image intensity is qualitatively expected due to the longer inelastic attenuation path of the wavefront that illuminates, and is subsequently scattered by, the backscattering atom, as compared to the wavefront paths that involve the side scattering atoms. Despite these

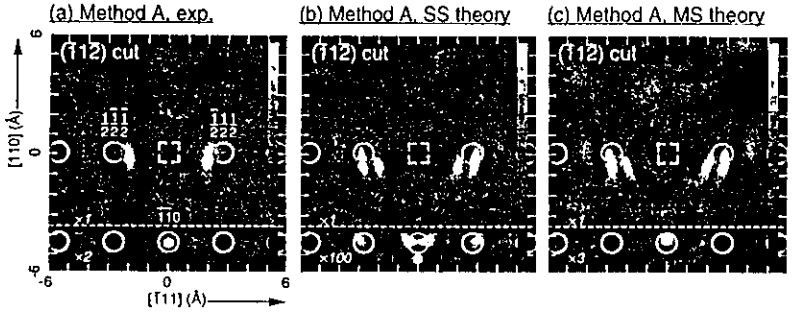

FIGURE 7. (a) W(110) atomic images obtained in the vertical $(\bar{1}\,1\,\bar{2})$ plane from experimental and theoretical W $4f_{7/2}$ surface emission $\chi(k)$ data sets, via (Eq. (6)). The surface emitter site is indicated by the dashed square, and the positions of the scatterers (assuming no surface relaxation) are indicated by circles. The nearest and next-nearest scattering positions have been labeled. Axes are marked off in 1Å units. Image intensities for $z \leq -3.5$Å have been rescaled, with the scale factors indicated on the figures. (a) Images reconstructed from the experimental $\chi(k)$ data set of Fig. 6(e). (b) Images reconstructed from a theoretical single scattering $\chi(k)$ data set. (c). Images reconstructed from a theoretical multiple scattering $\chi(k)$ data set.

position shifts and aberrations, this atomic image overall gives good *ab initio* estimates of the positions of the atoms surrounding the surface W(110) emitter, which could then be refined *e.g.*, using *R*-factor comparisons of experiment with model diffraction calculations for various structures.

The single and multiple scattering images of Figs. 7(b)-(c) are similar to experiment in that the $\frac{1}{2}\frac{\bar{1}}{2}\frac{\bar{1}}{2}$ and $\frac{\bar{1}}{2}\frac{1}{2}\frac{1}{2}$ side scatterers exhibit side lobes which are shifted in towards the emitter, and downward from the surface. However, the side scattering atomic images of Figs. 7(b)-(c) differ from those of Fig. 7(a) in that the theoretical image peaks are split. This splitting may be due to a number of reasons, among them the differences between the theoretical and actual wavenumber-dependent photoexcitation cross-sections, photoemitted source wave angular distributions, and atomic scattering factors. Still, these single- and multiple-scattering models produce other image features that rather closely match the experimental image of Fig. 7(a), even including the faint aberrations seen at $(x,z) \approx (\pm 4\text{Å}, 0\text{Å})$. The most marked difference between the experimental image of Fig. 7(a) and the single-scattering image of Fig. 7(b) is the triply-split backscattering $\bar{1}\,\bar{1}\,0$ atom in the latter, which is also very much weaker in intensity ($\approx$ 1%) relative to the $\frac{1}{2}\frac{\bar{1}}{2}\frac{\bar{1}}{2}$ and $\frac{\bar{1}}{2}\frac{1}{2}\frac{1}{2}$ image peaks. This is mainly due to the oversimplification of the single-scattering model, as seen by comparing Figs. 7(b) and (c). Note that in the multiple-scattering image of Fig. 7(c), the backscattering $\bar{1}\,\bar{1}\,0$ peak intensity relative to the side scattering $\frac{1}{2}\frac{\bar{1}}{2}\frac{\bar{1}}{2}$ and $\frac{\bar{1}}{2}\frac{1}{2}\frac{1}{2}$ image peaks ($\approx$ 33%) is more nearly that of Fig. 7(a) ($\approx$ 50%). This dramatic difference between single and multiple scattering can arise because each of the atoms in the multiple-scattering model becomes a secondary emitter, which can then illuminate the atoms surrounding them, especially the atom located at the $\bar{1}\,\bar{1}\,0$ relative position. In this way more scattering events contribute to the backscattering signal in the resulting holographic $\chi(\mathbf{k})$ intensities, and as such the reconstructed $\bar{1}\,\bar{1}\,0$ atomic intensity is much stronger for the image reconstructed from the multiple-scattering model than that from the single-scattering model. Thus, the closer match between Fig. 7(c) and the experimental image of Fig. 7(a) graphically illustrates that multiple-scattering more accurately describes the nature of the creation of the experimental holographic photoelectron intensities $I(\mathbf{k})$.

Atomic electron holography has been extensively tested on both bulk and surface structures, with some notable successes to date being the determination of structures of adsorbate overlayers (17c,19a,20a,27b-c,) and reconstructed surface structures (17e,19b). This technique is most useful in that initial atomic position estimates can be determined, which can then be refined using a more standard comparison of experiment and theory. Further improvements of image quality in atomic electron holography will lie primarily in the refinement of reconstruction kernels and algorithms that more accurately account for the non-ideal atomic scattering and propagation of electron wavefronts, as well as the wavenumber dependences and anisotropies in the source wave. Other holographic experiments that await implementation in the near future are the monitoring of temperature and coverage dependent structural phase changes; and spin-polarized photoelectron holography (SPPH) (35), where spin-specific photoemission (or detection) could be exploited to yield images of local atomic spin order.

ATOMIC X-RAY HOLOGRAPHY

In this section we review two experimental techniques for acquiring holographic x-ray data, and show the results of imaging experimental and theoretical x-ray holographic data sets involving both single and multiple wavenumbers.

The first atomic x-ray holographic images were recently obtained using what can be termed *x-ray fluorescence holography (XFH)*, as shown in Fig. 2(a). In this work, Tegze and Faigel (13) measured the hologram by monitoring the single-wavenumber Sr Kα emission ($k = 7.145\text{Å}^{-1}$, $E = 14.10$keV) from a single crystal of $SrTiO_3$. 2,402 intensities were measured over a full cone of 60° half angle above the surface. The final hologram was found to have anisotropies in intensity

of $\Delta I / I_0 \approx 0.3\%$. These much smaller effects mean that more demanding detector counting statistics are required in x-ray holographic measurements than with comparable atomic electron holography measurements. The reconstruction of this hologram via the optical kernel algorithm of Eq. (6) yields images of the Sr atoms only, as the much weaker scattering strength of the Ti and O atoms renders their images invisible compared to those of the Sr atoms. Figure 8(a) shows the experimental image reconstructed in the (010) plane (36), and it is compared in Fig. 8(b) to an image reconstructed from a theoretical $\chi(k)$ for Sr Kα emission from a simple-cubic Sr cluster of 27 atoms (14). The expected atomic image resolutions at this hologram wavenumber and angular range are $\delta x \approx 0.3$Å in the horizontal [100] direction, and $\delta z \approx 0.9$Å in the vertical [001] direction (34), and are roughly comparable to the atomic images of Figs. 8(a)-(b).

Reconstructing three-dimensional atomic images from a single-wavenumber hologram yields twin images. In any structure with inversion symmetry, these twins can overlap with real atomic images so as to confuse structural interpretation (37,38). In addition, the real and twin atomic images for a particular wavenumber and system can overlap completely out of phase, leading to an artificial suppression of atomic image intensities (37,38). It is thus advantageous to reconstruct direct atomic images from multiple-wavenumber $\chi(k)$ data sets so as to avoid such real-twin image overlaps (4a,4b,38). However, such XFH holograms cannot be measured at arbitrary wavenumbers, with the latter being limited by the intensity and number of fluorescence lines of the photoemitting species (38,39).

Another method for obtaining x-ray holographic information at conveniently chosen multiple wavenumbers has also very recently been demonstrated for the first time by Gog *et al.* (15,16), and its basic principle is illustrated in Fig. 2(b). This method has been termed *multiple energy x-ray holography* (MEXH). MEXH is the time-reversed version of the conventional geometry of XFH (Fig. 2(a)), in that the wave motions are reversed, and the emitter and detector positions are interchanged (Fig. 2(b)) (15,16,39,40). The exciting external x-ray beam now produces the reference and object waves, and the fluorescent atom acts only to detect the interference between the direct and scattered wavefronts in the near field. The emitted x-rays are now collected by a distant detector with a large acceptance solid angle, in principle yielding much higher effective counting rates. The far field source wave can be set to any wavenumber (energy) above the fluorescence edge of the emitting species. thus permitting holograms at multiple wavenumbers and yielding in principle atomic images with no real-twin image overlaps (15,16,39). Specifically, multiple-wavenumber x-ray holograms have been measured to date for hematite ($\alpha - Fe_2O_3(001)$) (15,40), and for Ge(001) (16).

We show the results of applying the optical kernel algorithm of Eq. (6) to experimental and theoretical MEXH data for $\alpha - Fe_2O_3(001)$ as measured by Gog and co-workers on Beamline X-14A of the National Synchrotron Light

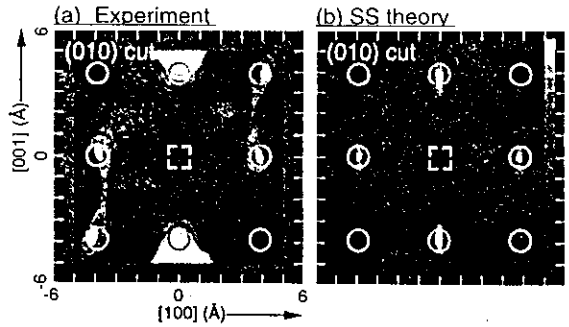

FIGURE 8. X-ray fluorescence holography atomic images of $SrTiO_3$ in the vertical (010) plane, obtained from (a) experimental (13) and (b) theoretical (14) Sr Kα $\chi(k)$ data sets, via Eq. (6). The Sr emitter site is indicated by the dashed square, and nearest-neighbor and next-nearest-neighbor Sr scatterers are indicated by circles. Axes are marked off in 1Å units.

Source at Brookhaven National Laboratory (15,40). Fe Kα fluorescence was excited by horizontally polarized radiation in the range $k = 4.561$Å^{-1} to 5.220Å^{-1} (E = 9.00keV to 10.30keV) that was incident on the $\alpha - Fe_2O_3(001)$ sample surface over a polar angle range of $60° \le \theta \le 90°$ = surface normal. These data points were measured at three wavenumbers with intervals of $\delta k \approx 0.329$Å^{-1} (δE = 650eV), and at angular intervals of $(\delta\theta,\delta\phi) = (5°,5°)$, making a total of 435 unique measurements in a symmetry-reduced 1/3rd of the total solid-angle above the sample. Figure 9(a) illustrates the orientation of the sample with respect to the horizontal ($\hat{e}_1$) polarization vector, with the vertical ($\hat{e}_2$) polarization vector shown also to permit discussing other possible experimental geometries. Figure 9(b) shows the raw measured $I(k)$ data set in k-space, as viewed down along $[00\bar{1}]$, in the same format as Figs. 6(b)-(d). Data points in the fourth quadrant have been cut away to reveal the $k = 4.561$Å^{-1} $I(k)$ intensities, while the other quadrants show the $k = 5.220$Å^{-1} $I(k)$ intensities. Note that the much weaker atomic scattering of x-rays renders the anisotropy of the raw $I(k)$ data ($\Delta I / I_0 \approx 0.5\%$) barely discernible with this linear gray scale.

Due to the limited wavenumber range of this $I(k)$ data set, a separate $I_0(k)$ was determined for each of the three different wavenumber holograms via a low-pass filter (34), thereby including in $I_0(k)$ the reference wave, as well as corrections for the effects of x-ray absorption during both excitation and emission. Figure 9(c) shows the normalized $\chi(k)$ obtained by this method from the raw $I(k)$ intensities of Fig. 9(b).

For comparison to the experimental results, a single-scattering model (38,41)

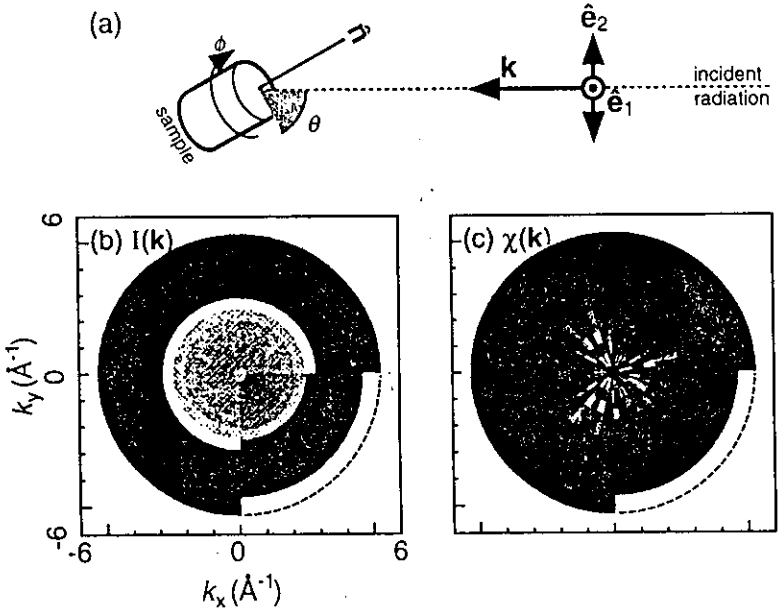

FIGURE 9. (a) Orientation of the sample (where $\hat{\mathbf{n}}$ is the surface normal) with respect to the horizontal ($\hat{\mathbf{e}}_1$) and vertical ($\hat{\mathbf{e}}_2$) polarization vectors of the incident radiation **k**. (b) Schematic k-space representation of the raw measured *I*(k) intensity data set for Fe Kα fluorescence from α-Fe_2O_3(001) excited by horizontally polarized radiation. (c) The normalized χ(k) data set. The format is the same as Figs. 6(b)-(d).

was used to calculate a theoretical $\chi(\mathbf{k})$ from an ideal $\alpha-Fe_2O_3(001)$ cluster containing 384 Fe atoms with two inequivalent Fe emitter sites as appropriate to the hematite lattice. The O atoms were not included due to their much smaller scattering power (15). The incident radiation in this model calculation is polarized horizontally with respect to the $\hat{\theta}$ and $\hat{\phi}$ rotation axes of the cluster (*cf.* Fig. 9(a)), as was the case in the measurement of the experimental *I*(k) data set discussed above. Because the incident radiation is polarized, the x-ray scattering factor in Fig. 5(a) must be further multiplied by the Thomson scattering factor, which has the form $\sin^2\Theta_{\varepsilon}^{\mathbf{k}'}$, where $\Theta_{\varepsilon}^{\mathbf{k}'}$ is the angle between the polarization vector of the incident radiation ε, and the direction **k'** of the scattered radiation. Thus, there will be nodes in the incoming scattered object waves along the polarization direction, and emitter atoms near this direction will not be strongly influenced by x-ray scattering. For the present case, the use of horizontal polarization is therefore a

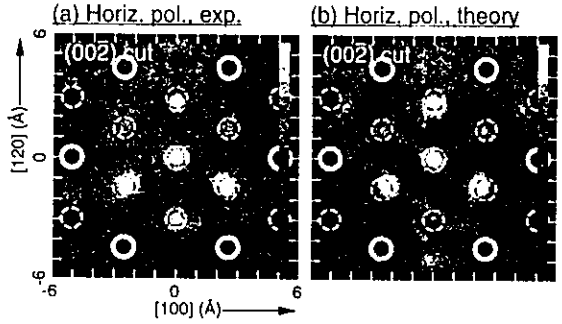

FIGURE 10. Multiple energy x-ray holography (MEXH) atomic images of α-Fe_2O_3(001) in the horizontal (00$\bar{2}$) plane situated 6.89Å below each of the two types of Fe emitters, obtained from (a) experimental and (b) theoretical Fe Kα χ(k) data sets, via Eq. (6). Fe scatterers in the bi-layer just above or below this plane are indicated by dashed circles, and Fe scatterers in relative positions common to both inequivalent Fe emitters are indicated by bold circles. Axes are marked off in 1Å units.

disadvantage in the imaging of horizontal planar structures such as those in $\alpha-Fe_2O_3(001)$, which is comprised of closely stacked horizontal Fe bi-layers with (001) orientation. The effect of such horizontally polarized incident radiation (via the Thomson cross section) is thus to strongly suppress atomic images in the basal (001) plane of the emitter, but to much less suppress images in horizontal planes farther above and below the emitter plane (40).

Figures 10(a) and (b) show the reconstructed atomic images in the (00$\bar{2}$) plane situated at z = -6.89Å below the emitter and obtained by applying Eq. (6) to the experimental and single-scattering theoretical $\chi(\mathbf{k})$ data sets, respectively. The expected image resolutions in the horizontal ([100] and [1$\bar{2}$0]) directions are $\delta x = \delta y \approx 0.6$Å (34). The experimental and theoretical images are very similar in that three of the Fe atoms from the neighboring upper bi-layer intrude into the (00$\bar{2}$) image plane. This intrusion is due to the limited wavenumber and angular range of the $\chi(\mathbf{k})$ data points in k-space (as compared to the larger wavenumber and angular range for the electron $\chi(\mathbf{k})$'s in the previous section), which results in atomic images much less resolved in the vertical [001] direction: $\delta z \approx 2.5$Å (34). Still, since these images are reconstructed from a multiple-wavenumber $\chi(\mathbf{k})$ data set, they should be freer of real-twin image overlaps (4,15,16,38-40).

As a future prospect, using unpolarized incident radiation in MEXH, or perhaps rotating the entire sample-detector complex by 90° so as to measure holograms with both horizontal polarization and vertical polarization (with the polarization vector in the plane formed by the azimuthal rotation axis (the normal

of the sample surface) and the x-ray incidence direction, would allow atomic images to be reconstructed for atoms in all horizontal and vertical planes.

In fact, however, there also exist some classes of structures where it would be sufficient to utilize horizontally polarized incident radiation, and for which vertical structural information is more important than horizontal planar structure. These include some surface structure problems and buried epitaxial atomic layers. We specifically illustrate what might be learned for a buried atomic layer by considering theoretically a single Ge "δ-layer" buried in Si(001) (40). The Ge atoms in the δ-layer are assumed to lie in horizontal epitaxial sites with respect to the surrounding Si(001), such that structural information in the horizontal plane of a Ge emitter is relatively unimportant compared to the possibly strained vertical distances between the Ge δ-layer atoms and the Si neighbors above and below them (42). Thus using horizontally polarized incident radiation to record a MEXH Ge Kα $\chi(\mathbf{k})$ data set for this system may prove to be sufficient, and perhaps even advantageous.

As an example, Figs. 11(a)-(c) show the Thomson scattering factors for unpolarized, horizontally polarized, and vertically polarized incident radiation, respectively. Figs. 11(d)-(f) show the reconstructed atomic images in the vertical $(1\bar{1}0)$ plane obtained from applying Eq. (6) to a theoretical single-scattering $\chi(\mathbf{k})$ data set calculated for these polarization modes (unpolarized, horizontally polarized, and vertically polarized) for an ideal Ge δ-layer buried in a Si(001) cluster with no vertical strain. These MEXH $\chi(\mathbf{k})$ intensities were calculated at 7 wavenumbers (energies) for radiation of $k = 6.081\text{Å}^{-1}$ to 9.122Å^{-1} ($E = 12.00$keV to 18.00keV) that was incident over a polar takeoff angle range of $10° \le \theta \le 90°$, and with wavenumber (energy) steps of $\delta k = 0.507\text{Å}^{-1}$ ($\delta E = 1.00$keV) and angle steps of $(\delta\theta,\delta\phi) = (5°,5°)$, yielding a total of 1,897 unique data points in the symmetry-reduced 1/4th of the total solid-angle above the cluster. The higher wavenumber and larger wavenumber and angular ranges of these MEXH $\chi(\mathbf{k})$ data sets ensure better resolved atomic images ($\delta x = \delta y \approx 0.2\text{Å}$; $\delta z \approx 0.4\text{Å}$) than those of Fig. 10 (34). The Ge δ-layer atoms are well-defined in the image obtained with unpolarized radiation (Fig. 11(d)), and the Si atoms in the layer directly above the Ge δ-layer are fairly well resolved, but the Si atoms in the top center of the image along the [001] direction are poorly resolved, being farther away from the emitter. In contrast, in the image obtained with horizontally polarized radiation (Fig. 11(e)), the Si atoms above and below the Ge δ-layer, including those at top center and bottom center of the image along the [001] direction, are clearly imaged compared to those in the basal plane of the Ge δ-layer. Thus, it appears that the strained vertical interlayer distances could be determined in an MEXH experiment on this system using horizontally polarized incident radiation. Figure 11(f) shows the image obtained with vertically polarized incident radiation, where in contrast to Fig. 11(e), the Ge δ-layer atoms are strongly evident, compared to the suppressed images of the Si atoms above and below. Should both vertical *and* horizontal

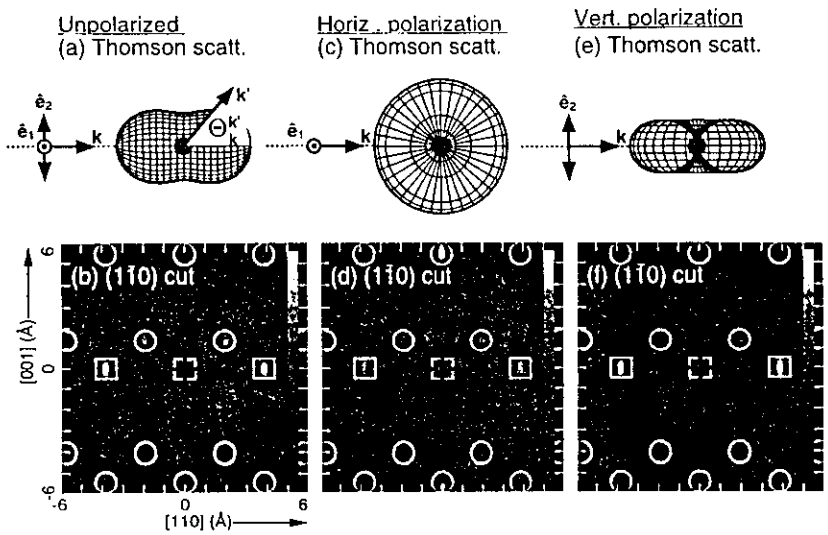

FIGURE 11. (a)-(c) Thomson scattering factors for unpolarized, horizontally polarized, and vertical polarized incident radiation, respectively. (d)-(f) Multiple energy x-ray holography images of a single Ge layer embedded in Si(001) (Si(001)/Ge-δ/Si(001)) in the vertical $(1\bar{1}0)$ plane obtained from theoretical Ge Kα $\chi(\mathbf{k})$ data sets via Eq. (6), for: unpolarized, horizontally polarized, and vertically polarized incident radiation, respectively. The Ge emitter site is indicated by the dashed square, and the Ge δ-layer scatterers are indicated by solid squares. The Si atoms directly above and below the Ge δ-layer are indicated by circles. Axes are marked off in 1Å units.

structural information be desired for a given system with only linearly polarized incident radiation for excitation, then $\chi(\mathbf{k})$ intensities measured using horizontally and vertically polarized radiation separately could simply be added to determine the MEXH $\chi(\mathbf{k})$ intensities for most of the solid angle above the sample that one would measure using unpolarized incident radiation (40). The use of circularly polarized incident radiation should also be advantageous in this respect (40). In order to determine the vertical strain in this system (an effect of a few percent), increased spatial resolution of atomic images could be obtained by measuring holographic $\chi(\mathbf{k})$ intensities at higher wavenumbers (34).

Thus atomic x-ray holography holds much promise for the imaging of local atomic structure surrounding a specific emitter species of interest. The more ideal atomic scattering nature of x-rays produces reconstructed images that are relatively free of the aberrations, artifacts, and position shifts that are usually found in comparable electron atomic holographic images. XFH and MEXH also share

the advantage of being element specific; thus the local structure around each atomic type in a sample can be determined. In addition, neither XFH or MEXH requires a sample with long range crystalline order; it need only be minimally ordered to within the potential imaging volume surrounding the emitter site that can be resolved with the k-space resolution of a given $\chi(\mathbf{k})$ data set (30,38). In contrast to the bulk structures considered in the initial implementation of this technique, atomic x-ray holography would be advantageously used to image structures with only short-range order which cannot be determined using conventional x-ray diffraction probes, such as surface and buried atomic layers; strained atomic lattice positions surrounding dopant sites (Fig. 12(a)); as well as

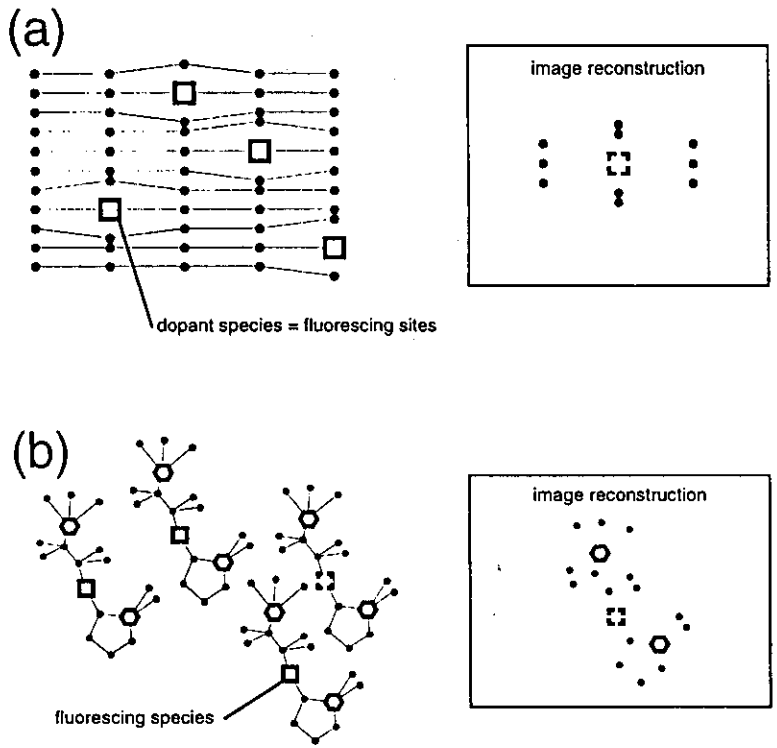

FIGURE 12. Schematic representation of two types of short-range-order atomic structures that could be fruitfully studied using atomic x-ray holography, together with their expected reconstructed images. (a) Strained lattice atoms surrounding dopant sites. (b) Rotationally aligned macromolecules with poor long-range translational symmetry.

the structure of macromolecules which do not exhibit perfect translational symmetry in crystal form (Fig. 12(b)). But one can also imagine using x-ray holography as a adjunct to conventional x-ray diffraction, with good estimates of local structures and phase relationships being derived to assist the diffraction analysis. Exploitation of linear and circularly polarized incident radiation in MEXH may also be utilized to emphasize horizontal and/or vertical structures of interest.

CONCLUDING REMARKS

In conclusion, holographic atomic imaging with localized single-atom sources of electrons or x-rays promises to become an important structural probe that will complement, or in some respects even surpass, conventional diffraction methods or other atomic structure probes. These holographic methods should be applicable to a wide variety of systems of practical and fundamental interest. X-ray holography of either the single-wavenumber fluorescence type or the multiple-wavenumber (inverse) type promises to yield more accurate images due to the more ideal scattering of x-rays, although the much weaker diffraction effects observed with x-rays also present challenges in measurement. However, with brighter sources of x-rays at next-generation synchrotron radiation facilities, and the development of faster detectors, these experimental problems should be surmountable. Thus, although much experimental and theoretical work lies ahead if we are to develop both the electron and x-ray techniques to their fullest potential, the final fulfillment of Gabor's dream for atomic-resolution holography seems well worth the effort.

ACKNOWLEDGEMENTS

Research at UC-Davis was supported in part by the Office of Naval Research (Contract Nos. N00014-90-5-1457 and N00014-94-1-0162), by the Director, Office of Energy Research, Office of Basic Energy Sciences, Materials Sciences Division of the U. S. Department of Energy (Contract No. DE-AC03-76SF00098), the National Energy Research Supercomputer Center, and by the International Centre for Diffraction Data. The authors would like to thank T. Gog, J. D. Denlinger, E. Rotenberg, F. Arfelli, R. A. Eisenhower, A. P. Kaduwela, R. H. Menk, D. Novikov, and S. Thevuthasan for their experimental and theoretical collaborative efforts, and M. A. Van Hove and R. L. Johnson for their useful comments during the preparation of this manuscript. Use of a preliminary version of a new multiple-scattering photoelectron diffraction program package was made possible by Y. Chen, H. Wu, and D. A. Shirley.

REFERENCES

1. Gabor, D. *Nature* (London) **161**, 777-778 (1948).
2. Wolf, E. *Optics Communications* **1**, 153-156 (1969), and *Optical Society of America* **60**, 18-20 (1970).
3. Syms, R. R. A., *Practical Volume Holography*, Oxford: Clarendon Press, 1990, ch. 1, pp. 21-28.
4. (a) Barton, J. J., *Physical Review Letters* **61**, 1356-1359 (1988), and *Physical Review Letters* **67**, 3106-3109 (1991). (b) Barton, J. J., and Terminello, L. J., paper presented at the Third International Conference on the Structure of Surfaces, Milwaukee, July 1990, and in *Structure of Surfaces III*, S. Y. Tong, M. A. Van Hove, X. Xide, and K. Takanayagi, eds., (Springer Verlag, Berlin, 1991) p. 107. (c) Tong, S. Y., Huang, H., and Wei, C. M., *Physical Review B* **46**, 2452-2459 (1992), and references therein.
5. Szöke, A., *Short Wavelength Coherent Radiation: Generation and Applications*, T. Attwood, J. Boker (eds.), AIP Conference Proceedings No. 147, (AIP, New York, 1986) pp. 361-367.
6. Karla, J., and Hauptmann, H. A., *Acta Crystallographica* **3**, 18 (1950).
7. Lipscomb, W. N., *Acta Crystallographica* **2**, 193 (1949).
8. Hümmer, K., Billy, H., *Acta Crystallographica A* **38**, 841 (1982).
9. Chang., S., L., *Physical Review Letters* **48**, 163 (1982).
10. Hutton, J. T., Trammell, G. T., and Hannon, J. P., *Physical Review B* **31**, 743 (1985), and *Physical Review B* **31**, 6420 (1985).
11. Bedyzk, M. J., and Materlik, G., *Physical Review B* **32**, 6456 (1985).
12. Saldin, D. K., Harp, G. R., Tonner, B. P., *Physical Review B* **45**, 9629 (1992).
13. Tegze, M., and Faigel, G., *Nature* **380**, 49-51 (1996).
14. Fadley, C. S., and Len, P. M., *Nature* **380**, 27-28 (1996), and unpublished results.
15. Gog, T., Len, P. M., Materlik, G., Bahr, D., Sanchez-Hanke, C., and Fadley, C. S., *Physical Review Letters* **76**, 3132-3135 (1996).
16. Gog., T., Menk, R.-H., Arfelli, F., Len, P. M., Fadley, C. S., and Materlik, G., *Synchrotron Radiation News* **9**, 30-35 (1996).
17. (a) Terminello, L. J., Petersen, B. L., and Barton, J. J., *Journal of Electron Spectroscopy and Related Phenomena* **75**, 229-308 (1995), and references therein. (b) Wu, H., Lapeyre, G. J. Huang, H., and Tong, S. Y., *Physical Review Letters* **71**, 251-254 (1993) and references therein. (c) Zharnikov, M., Weinelt, M., Zebisch, P., Stichler, M., Steinrück, H.-P., *Surface Science* **334**, 114-134 (1995), and references therein. (d) Denecke, R., Eckstein, R., Ley, L., Bocquet, A. E., Riley, J. D., Leckey, R. C. G., *Surface Science* **331-333**, 1085-1092 (1995). (e) Tobin, J. G., Waddill, G. D., Li, H., Tong, S. Y., *Surface Science* **334**, 263-275 (1995), and references therein.
18. (a) Li, H., Tong, S. Y., Naumovic, D., Stuck, A., and Osterwalder, J., *Physical Review B* **47**, 10036-10039 (1993). (b) Saldin, D. K., Harp, G. R. and Chen, X., *Physical Review B* **48**, 8234-8245 (1993), and references therein.
19. (a) Han, Z.-L., Hardcastle, S., Harp, G. R., Li, H., Wang, ,X.-D. Zhang, J., and Tonner, B. P., *Surface Science* **258**, 313-327 (1991), and references therein. (b) Hong, I. H., Shyu, S. C., Chou, Y. C., and Wei, C. M., *Physical Review B* **52**, 16884-16891 (1995), and references therein.
20. (a) Mendez, M. A., Glück, C., Guerrero, J., Andres, P. L., Heinz, K., Saldin, D. K., and Pendry, J. B., *Physical Review B* **45**, 9402-9405 (1992), and references therein. (b) Wei, C. M., Tong, S. Y., Wedler, H., Mendez, M. A., and Heinz, K., *Physical Review Letters* **72**, 2434-2437 (1994), and references therein.
21. Tong, S. Y., Huang, H., and Guo, X. Q., *Physical Review Letters* **69**, 3654-3657 (1992).
22. Saldin, D. K., Harp, G. R., Chen, B. L., and Tonner, B. P., *Physical Review B* **44**, 2480-2494 (1991).
23. (a) Thevuthasan, S., Herman, G. S., Kaduwela, A. P., Tran, T. T., Kim, Y. J., Saiki, R. S., and Fadley, C. S., *Journal of Vacuum Science and Technology A* **10**, 2261-2270 (1992). (b) Herman, G. S., Thevuthasan, S., Tran, T. T., Kim, Y. J., and Fadley, C. S., *Physical Review Letters* **68**, 650-653 (1992). (c) Tran, T. T., Thevuthasan, S., Kim, Y. J., Friedman, D. J., Fadley, C. S., *Physical Review B* **45**, 12106-12109 (1992), and *Surface Science* **281**, 270-284 (1993). (d) Thevuthasan, S., Ynzunza, R. X., Tober, E. D., Fadley, C. S., Kaduwela, A. P., and Van Hove, M. A., *Physical Review Letters* **70**, 595-598 (1993).
24. Hu, P. and King, D. A., *Physical Review B* **46**, 13615-13618 (1992).
25. Tonner, B. P., Han, Z.-L., Harp, G. R., and Saldin, D. K., *Physical Review B* **43**, 14423-14433 (1991).
26. Thevuthasan, S., Ynzunza, R. X., Tober, E. D., Fadley, C. S., Kaduwela, A. P., and Van Hove, M. A., *Physical Review Letters* **70**, 595 (1993).
27. (a) Tong, S. Y., Li, H., and Huang, H., *Physical Review B* **51**, 1850-1854 (1995). (b) Wu, H., and Lapeyre, G. J. *Physical Review B* **51**, 14549-14553 (1995). (c) Roesler, J. M., Sieger, M. T., and Chiang, T.-C., *Surface Science* **329**, L588-592 (1995), and references therein.
28. Rous, P. J. and Rubin, M. H., *Surface Science* **316**, L1068-1074 (1994).
29. Hofmann, P., Schindler, K.-M., Fritzsche, V., Bao, S., Bradshaw, A. M., and Woodruff, D. P., *Journal of Vacuum Science and Technology A* **12**, 2045-2050 (1994), *Surface Science* **337**, 169-176 (1995), and references therein.
30. (a) Len, P. M., Thevuthasan, S., Kaduwela, A. P., Van Hove, M. A., and Fadley, C. S., *Surface Science* **365**, 535-546 (1996). (b) Len, P. M., Zhang, F., Thevuthasan, S., Kaduwela, A. P., Van Hove, M. A., and Fadley, C. S., *Journal of Electron Spectroscopy and Related Phenomena* **76**, 351-357 (1995). (c) Len, P. M., Zhang, F., Thevuthasan, S., Kaduwela, A. P., Fadley, C. S., and Van Hove, M. A., submitted to the *Journal of Electron Spectroscopy and Related Phenomena.*
31. Denlinger, J. D., Rotenberg, E., Len, P. M., Kevan, S. D., Tonner, B. P., and Fadley, C. S., in preparation.
32. Ynzunza, R. X., private communication.
33. SCAT photoelectron diffraction program package, Chen, Y., Wu, H., and Shirley, D. A., private communication.
34. Harp, G. R., Saldin, D. K., Chen, X., Han, Z.-L., and Tonner, B. P., *Journal of Electron Spectroscopy and Related Phenomena* **57**, 331-355 (1991).
35. (a) Timmermans, E. M. E., Trammell, G. T., and Hannon, J. P., *Physical Review Letters* **72**, 832-835 (1994). (b) Kaduwela, A. P., Wang, Z., Thevuthasan, S., Van Hove, M. A., and Fadley, C. S., *Physical Review B* **50**, 9656-9659 (1994).
36. Faigel, G., private communication.
37. Tegze, M., Faigel, G., *Europhysics Letters* **16**, 41-46 (1991).
38. Len, P. M., Thevuthasan, S., Fadley, C. S., Kaduwela, A. P., and Van Hove, M. A., *Physical Review B* **50**, 11275-11278 (1994).
39. Len, P. M., Gog, T., Fadley, C. S., and Materlik, G., submitted to *Physical Review B.*
40. Len, P. M., Gog, T., Novikov, D., Eisenhower, R. A., Materlik, G., and Fadley, C. S., submitted to *Physical Review B.*
41. *International Tables for X-ray Crystallography*, edited by K. Lonsdale (Reidel, Dordrecht, 1968), Vol. III.
42. Falta, J., Gog, T., Materlik, G., Muller, B. H., and Horn-von Hoegen, M., *Physical Review B* **51** 7598-7602 (1995), and references therein.